# An Integrated Toolbox for Image Registration, Fusion and Classification

**Markus Neteler**[*], **Daniel Grasso**[**], **Ivan Michelazzi**[**], **Luca Miori**[**], **Stefano Merler**[*] and **Cesare Furlanello**[*]

[*]   ITC-irst, Via Sommarive, 18, 38050 Povo (Trento), Italy

    Tel: +39-0461-314-520    Fax: +39-0461-314-591    E-mail: neteler@itc.it

[**]  University of Trento, 38050 Povo (Trento), Italy

**Abstract**

*In this paper we present a suite of new image processing tools for the GRASS Geographic Information System. New modules are suggested to support improved and semi-automated geocoding of vertical imagery. The ortho-rectification procedures have been extended to rectify oblique imagery from digital hand-held cameras for rendering purposes. Multi- and hyperspectral image analysis has been implemented to derive landuse/landcover maps at subpixel resolution. Image fusion with the Brovey transform is shown. We finally show high performance SMAP image classification on an openMosix cluster.*

## 1. Introduction

Remote sensing at various scales plays a major role in spatio-temporal earth surface monitoring. A wide range of satellite platforms as well as film and digital aerial photography provide a huge data repository. The full integration of remote sensing tools into a full Geographic Information System (GIS) provides a major advance over stand-alone solutions. The Open Source/Free Software GIS GRASS (http://grass.itc.it) has had significant image processing capabilities for years, and is now chosen as the framework for further enhancement through implementation of the image processing toolbox. The existing methods have been extended by integrating new geocoding algorithms for semi-automated registration of aerial imagery and oblique images from hand-held digital cameras. An image fusion algorithm for imagery from satellites or digital aerial cameras was included. Spectral unmixing as method to derive thematic maps at subpixel accuracy was integrated for multi- and hyperspectral data. Finally the usage of a powerful

image classification on an *openMosix* based cluster is show in this paper (Figure 1).

## 2. Image Registration

While image registration support has been present in GRASS (Neteler and Mitasova, 2004) for many years, there have been some restrictions in the flexibility of the provided tools. A basic problem is the time consuming manual identification of ground control points (GCPs). To overcome this problem, two new methods have been implemented which address the GCP identification within time-distant images as well as the semi-automatisation of the GCPs search.

### 2.1 Image Registration by Homography

Image registration of heterogeneous data sources such as historical images and present-day orthophotos often turns out to be complicated due to differences in survey time, camera type and the evolution of the observed landscape. The search of ground control points becomes very time consuming and may be even impossible for
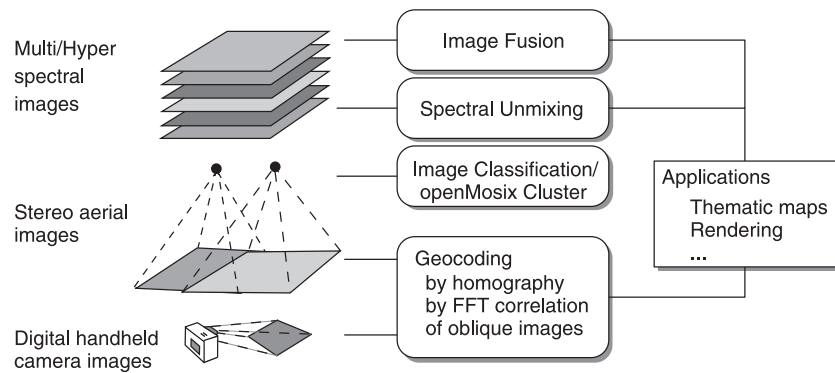
Figure 1: New image processing tools integrated into GRASS GIS

some part of the image scene. The common way of registering images is to find corresponding points (GCPs). An alternative method is the selection of corresponding lines. Linear structures are more easily identifiable by human eye than point structures (Chambers et al., 1983). In case of image registration of historical images, substantial changes in the landuse/landcover may render point identification to be impossible while linear structures such as bridges, streets, and railroads still can be selected. A combined method has been implemented in the new modules *i.linespoints* which permits identification of common ground control points in combination with corresponding lines. A subsequent run of the new module *i.homography* allows for homography based image rectification (Grasso, 2004). Homography is a simple linear projective transformation of four known points in one planar system $(x, y)$ to another planar reference system $(x', y')$. Thus, this transformation is applicable only to images covering flat terrain. In the new *i.linespoints,* the transformation, which was originally developed for points only, has been extended to homogeneous equations which describe a line $(t, u)$. To unify the two techniques, we developed a method which gives a different weight to points and lines (extending the approach of Murino et al., 2002) according to a weighting parameter $c$. To minimize the transformation error, the Brent minimization

algorithm was used to optimize the parameter $c$. Another related method to calculate the mean error was implemented in order to provide this value to the user for both points and lines types. Additionally, a test set of independent points can be specified and transformed to verify the overall quality of the rectification for other parts of the image scene. Figure 2 illustrates the selection of corresponding lines in very heterogeneous images with *i.linespoints*. The subsequent use of *i.homography* rectifies the image to the target GRASS location.

### 2.2 Semi-Automated Image Registration by Fast Fourier Transform

The classical image registration is done by searching a certain number of corresponding points (ground control points, GCPs) between two images. One image is selected as reference image. Corresponding points are then selected to define a transformation function, usually a polynomial, to rectify the unregistered image. In current GRASS versions, these GCPs have to be identified manually. We propose a new module *i.coregister* which provides an alternative, semi-automated approach to find corresponding points in two overlapping images (Miori, 2004). GCPs are found by maximising the cross-correlation within master-slave search windows between the two images. The cross-correlation is calculated by a frequency analysis of the

52

Fourier transformed search windows. In order to obtain high registration accuracy, first two regions are roughly indicated on screen by mouse, with very general requirements to image dimensions and overlapping zone characteristics. After determining the size of these search windows ($S_d$, Figure 3), the search window jump distance ($S_j$, offset in pixel when moving the search window) and the search window border ($S_b$, minimum distance to keep from border, set to $S_d/2$) the algorithm searches for the shift maximising the cross-correlation between the two search windows. Let $I_1 (x, y)$ and $I_2 (x, y)$ be the current master and slave search windows respectively. The cross-correlation is defined as

$$H(t_1, t_2) = \int_{S_r} I_1 (x, y) I_2 (x + t_1, y + t_2) d\mu, \qquad \text{Equation 1}$$

where $S_r$ is the search region and $t_1$ and $t_2$ represent the horizontal and vertical shifts respectively. The convolution theorem allows us to compute the cross-correlation in terms of the Fourier Transforms of $I_1$ and $I_2$:

$$H(t_1, t_2) = \Im^{-1} (\Im(I_1) \Im^*(I_2)), \qquad \text{Equation 2}$$

where $\Im$ indicates the Fourier Transform and $\Im^*$ the complex conjugate. The position of the maximum correlation value, $(\bar{t}_1, \bar{t}_2) = \max_{(t_1, t_2)} H (t_1, t_2)$,
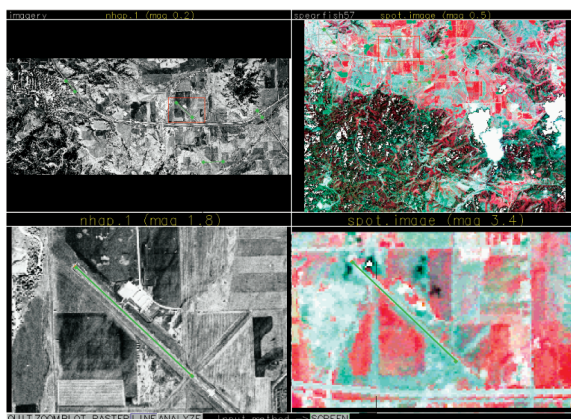


Figure 2: Image registration with homography: Selecting corresponding lines with *i.linespoints* (left: NHAP, right SPOT MSS)

determines the position of the GCP for the current pair of master/slave search windows. The set of GCPs is saved into the common GRASS POINTS structure for later use with *i.rectify.* Figure 4 shows an example for the automated search of GCPs by cross-correlation in a user-defined search region. The list of GCPs generated by *i.coregister* can optionally be converted into the 3D POINTS structure of *i.ortho. photo* by a new script *i.pointsfile2orthopoints-file.sh* which merges the POINTS file with a user specified camera file and elevations which are automatically queried from a DEM.

## 2.3 Image Registration of Oblique Aerial Photos from Digital Hand-Held Cameras

A new application of the *i.ortho.photo* algorithm is proposed for the registration of oblique imagery as produced by handheld digital cameras (Michelazzi, 2004). The underlying idea is to improve the visual perception of perspective rendering based on orthophotos. While oblique rendering using a digital elevation model and orthophotos usually suffers from perspective displacements, we show that digital photos taken by cheap digital cameras can be geocoded and used to improve the visual perception. The existing ortho-rectification algorithm has been tested for

usage of digital images which are lacking fiducial marks;

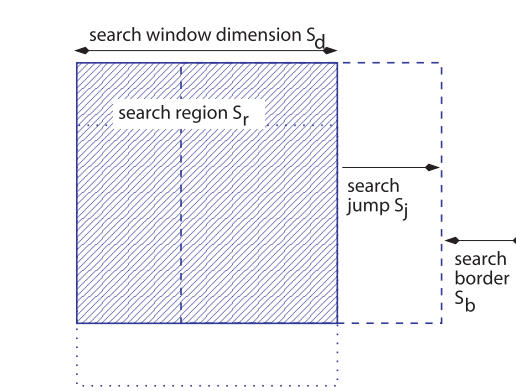estimation of the focal length of digital hand-held cameras;



Figure 3: Definition of search windows in FFT based image correlation *(i.coregister)*

estimation of exterior orientation of oblique photographs taken by a digital hand-held camera.

Most digital hand-held cameras create photos in JPEG format with EXIF (Exchangeable Image File) extension which stores metadata of the camera. Using a JHEAD EXIF JPEG camera setting parser (JHEAD EXIF JPEG camera setting parser, http://www.sentex.net/~mwandel/jhead/) camera parameters can be extracted, such as shutter speed, the distance the camera was focused at, focal length and the calculated 35 mm equivalent focal length, image size and resolution, the time and date the picture was taken, as well as the camera maker and model. The estimation of the parameters of the exterior orientation is done using the "Space Resection by Collinearity" method following the approach of Wolf, 1983. Space Resection is a method of determining the six elements of exterior orientation of a single tilted photograph. Based on least squares techniques the most probable values for the six elements are determined. In order to rectify an oblique image with *i.ortho. photo,* the following modifications to the standard procedure have to be applied:

the focal length is taken from the JHEAD output;

the number of fiducial marks is set to four, their positions are centred on each side of the photo. To get the position in millimetres, the relation between the longer and the shorter side of the photo is considered (in case of a non-quadratic photo), as well as the resolution versus the photo size in pixels;

initial parameters for the exterior orientation have to be estimated and entered into the related screen of *i.ortho.photo:*

the x, y, z coordinates of the camera position can be easily estimated from DTM with *d.what.rast* or the "What's here" functionality of *nviz;*

the orientation angles (omega, phi, kappa) of the camera can be estimated with *d.measure;*

the ground control points are identified as usual. However, the user has to take care to select appropriate points in both the oblique photo and the map/orthophoto reference (usually object corners).

Finally the ortho-rectification is performed. A detailed report of the parameter estimation can be obtained by recompilation of *i.ortho. photo* with debug option enabled. Figure 5 shows an example for the registration of an oblique photo.



Figure 4: Automated search of GCPs by cross-correlation in a user-defined search region *(i.coregister)*

## 3.  New Image Classification Tools with Subpixel Accuracy

In this section of the paper, we present two methods for analysing multi- and hyperspectral data. Hyperspectral sensors divide the waveband-range of interest into hundreds of contiguous narrow bands. This spectral sampling is then subject to signature analysis, usually based on a spectral library containing a large set of laboratory spectra or on geometrical search for pure spectra in the image scene itself. The data in each pixel can be understood as a cube of two spatial dimensions and a third spectral dimension, the wavelength. One or many objects are covered by a pixel, resulting in mostly mixed spectral signals of objects within each pixel. A common model to describe these mixed signals is assumption of linear mixing (linear mixture model, LMM). The methods of spectral angle mapping and spectral unmixing decompose the mixed signal into a set of known spectra (endmembers) from the spectral library. This results in a classifier with subpixel accuracy as for each endmember an abundance map is produced. Difficulties arise from various factors such as dependence on sun angle, atmospheric absorption and scattering, reflections and shadowing, as well as spatial and spectral aberrations in the sensor (Shaw and Manolakis, 2002).

### 3.1 Spectral Angle Mapping

Spectral angle mapping has been implemented in the new module *i.spectral.sam* (Neteler, 1999). For a set of bands the algorithm is calculating the angles to a set of object spectra which are read from a spectral library. SAM is invariant to unknown multiplicative scalings and, consequently, is invariant to unknown deviations that may arise from different illumination and angle orientation (Keshava and Mustard, 2002). Details are explained in the next section, see Equation 12.

### 3.2 Spectral Unmixing

Spectral unmixing for landuse/landcover mapping at subpixel precision has been imple-

mented in the module *i.spectral.unmix* (Neteler, 1999). Multi- and hyperspectral data can be analysed against a spectral library (e.g. USGS Digital Spectral Library, http://speclab.cr.usgs.gov/spectral-lib.html; ASTER spectral library, http://speclib.jpl.nasa.gov). The module generates as many abundance maps as object spectra are used. The implemented algorithm assumes the linear mixture of object spectra (also called "endmembers") within each pixel. The general case is a set of linear equations with $m$ equations and $n$ endmember spectra (Shimabukuro and Adams, 1991). The number of equations $m$ is identical to the number of bands of the sensor. The fractions of endmembers represent the percentage of landuse/landcover within the actual pixel. The number of endmember which can be extracted is as high as the number of bands. Written as a general system of equations:

$$
\begin{aligned}
a_{11}x_1 + a_{12}x_2 + ... + a_{1n}x_n &= b_1 \\
a_{21}x_1 + a_{22}x_2 + ... + a_{2n}x_n &= b_2 \\
&\vdots \qquad\qquad\qquad\qquad \text{Equation 3}\\
a_{m1}x_1 + a_{m2}x_2 + ... + a_{mn}x_n &= b_n
\end{aligned}
$$

The rows correspond to the bands ($m$ bands) and the columns to the endmember spectra ($n$ endmembers). The constants $a_{ij}$ represent the reflection value in the ith band (i in 1, ... ,$m$) of the $j_{th}$ object (j in 1, ... , $n$). The percentage of an endmember fraction within a pixel is $x_j$ while $b_i$ describes the overall pixel value of the $i$th band. This can be rewritten as:

$$
\begin{pmatrix}
a_{11} & a_{12} & ... & a_{1n} \\
a_{21} & a_{22} & ... & a_{2n} \\
\vdots & \vdots & \vdots & \vdots \\
a_{m1} & a_{m2} & ... & a_{mn}
\end{pmatrix}
\begin{pmatrix}
x_1 \\ x_2 \\ \vdots \\ x_n
\end{pmatrix}
=
\begin{pmatrix}
b_1 \\ b_2 \\ \vdots \\ b_m
\end{pmatrix}
$$

Equation 4

and simplified to:

$$Ax = b. \qquad\qquad \text{Equation 5}$$

Here $A$ indicates the matrix of reference spectra, the vector $x$ the percentage fraction of spatial distribution within the pixel, and the vector

55

*b* the pixel values in the image scene. To solve this system of equations, it is required that $m \geq n$, which means that the number of objects to be analysed must be lower or as much as the number of bands available. In case of $m=n$ the matrix *A* is quadratic. An additional condition is that the equations should be linearly independent. The unknown vector *x* can be calculated as:

$$x = A^{-1}b. \qquad \text{Equation 6}$$

But to get physically meaningful results, we must enforce two boundary conditions: First, the sum of all fractions must be 100% (full additivity, assuming the case that at least one reference spectrum is found in each pixel):

$$\sum_{j=1}^{n} x_j = 1. \qquad \text{Equation 7}$$

Secondly, the area fractions must be zero or positive (non-negativity):

$$x_j \geq 0 \text{ for all } j. \qquad \text{Equation 8}$$

The ideal solution of the rewritten Equation 6 is zero:

$$A^{-1}b - x = 0, \qquad \text{Equation 9}$$

but due to limitations in the accuracy of the reference spectra, limitations in the assumption of linear mixture and natural deviations of the object spectra from the reference spectra, the Equation 6 cannot be solved exactly. To overcome this problem, an error term is introduced to cover the unidentifiable object spectra and noise:

$$A^{-1}b - x = \varepsilon. \qquad \text{Equation 10}$$

Because vector *x* and error $\varepsilon$ are unknown, the equation can be solved by minimizing the error through least-squares. The error function *F* to be minimised can be written as:

$$F = \sum_{i=1}^{m} \varepsilon_i^2. \qquad \text{Equation 11}$$

With minimisation of the error function *F,* the vector *x* which represents the percentage fraction of the reference spectra in the actual pixel can be calculated from Equation 5. The methods have been implemented to calculate the area fractions $x_j$ while minimising the error and respecting the two boundary conditions as given in Equation 7 and Equation 8. It is recommended to beforehand test the matrix of reference spectra *A* for linear dependencies using Spectral Angle Mapping (SAM). In this case the selected spectra should be exchanged from the matrix to improve the spectral separability. This is obtained by calculating the angle $\varphi$ between column vector $a_j$ and $a_{j+1}$ in the matrix, i.e. between individual reference spectra (Sohn and McCoy, 1997):

$$\varphi = \cos^{-1}\left( \frac{a_j^T a_{j+1}}{\|a_j\|_2 \cdot \|a_{j+1}\|_2} \right), \qquad \text{Equation 12}$$

where $\|a\|_2$ is the Euclidean norm of *a*.

The length of the vectors represents the signal power, i.e. the reflectivity of the observed object surface. If the spectra are too close, i.e. the angle $\varphi$ is too small, a spectral separation cannot be performed. In this case the vectors are linearly dependent. Less noise and a higher number of bands minimises the problem. A mathematical problem arises from the inversion of matrix *A* (Equation 6 and Equation 9). Due to limits in the sensor signal and other noise, only ill conditioned matrices are expected; classical matrix inversion methods such as Gauss elimination or LR decomposition will fail here. The singular value decomposition (SVD) proposed by some authors is also inappropriate as it does not fulfill the second boundary condition (Equation 8). While enforcing the first (sum of areas be 100%) and the second (all area percentages within the positive range, compare Equation 8) boundary conditions, the implemented algorithm iteratively minimses the error $\varepsilon$ (constraint least square method, Shimabukuro and Adams, 1991). The solution of the equation is projected from the undesired negative solution space to the boun-

dary of the desired positive solution space (Sohn and McCoy, 1997; Hobbs, 1996:8).

To solve the set of equations, the gradient of the error function $F$ (Equation 11) is considered. In a multidimensional feature space the function $F$ is a hyper-parabola. A three-dimensional case for two spectral bands is shown in Figure 7. The error surface for this example is calculated as:

$$F = \left\| (Ax - b) \right\|_2^2 = (Ax - b)^T (Ax - b)$$

$$\text{Equation 13}$$

The numerically optimal solution $x$ would be the minimum of the error function, but it violates the boundary conditions. In the proposed algorithm, a vector $x$ is initialized to a seed value. The set of seed values initially defines an equivalent area fraction for each endmember
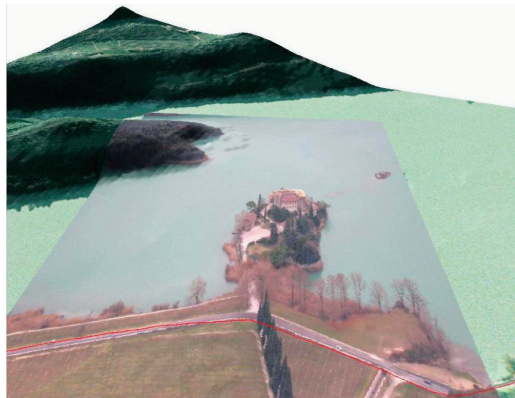


Figure 5: Perspective rendering of an oblique photo taken by a digital hand-held camera (registered by *i.ortho.photo*), the photo is draped over an orthophoto
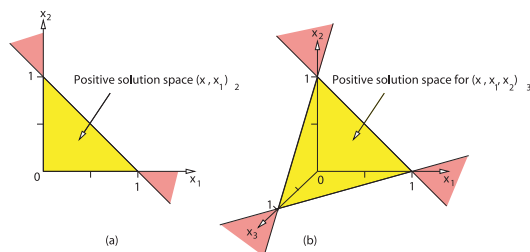


Figure 6: Permitted (bright) and undesired (dark) negative solution space of a two-dimensional (a) and of a three-dimensional spectral unmixing (b) with constraints (after Sohn and McCoy, 1997)
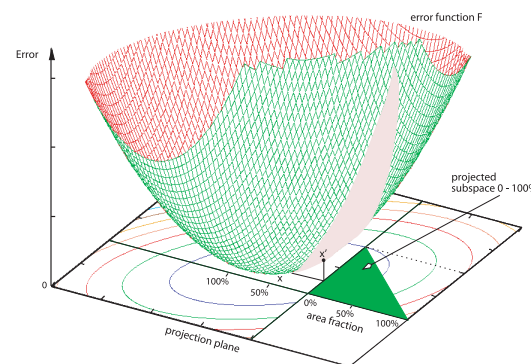
and these fractions are put into Equation 9. Using the approach of steepest descent the calculated error can be minimised. To do so, the values of the vector $x'$ are shifted by the small value $\mu$ in the direction of decreasing slope of the error function. The gradient at position $k$ on the error surface $F$ is calculated as (Harteneck 1998, pers. comm.):

$$\frac{\partial F}{\partial x} = 2A^T (Ax'(k) - b) \qquad \text{Equation 14}$$

The new vector $x'(k+1)$ is calculated for an increment $\mu$ as:

$$x'(k+1) = x'(k) - \mu \cdot 2A^T (Ax(k) - b)$$

$$\text{Equation 15}$$

In the next iteration the new vector $x$ will be inserted again into Equation 9, which determines a new error value. This will lead to a corrected vector $x'$. We finish the loop when we leave the positive solution space or when we reach the minimum of the error function. The



Figure 7: Example for error function $F$, as calculated for a pixel in spectral unmixing of two bands. The figure depicts the case of a numerically correct solution for fraction $x$ in the negative range. However, this minimum solution is outside the boundary conditions. The physically desired solution $x$ lays within the range of 0% to 100% (triangle on error surface) and is found by projecting into the positive range while keeping $x'$ as close as possible to error minimum at $x$
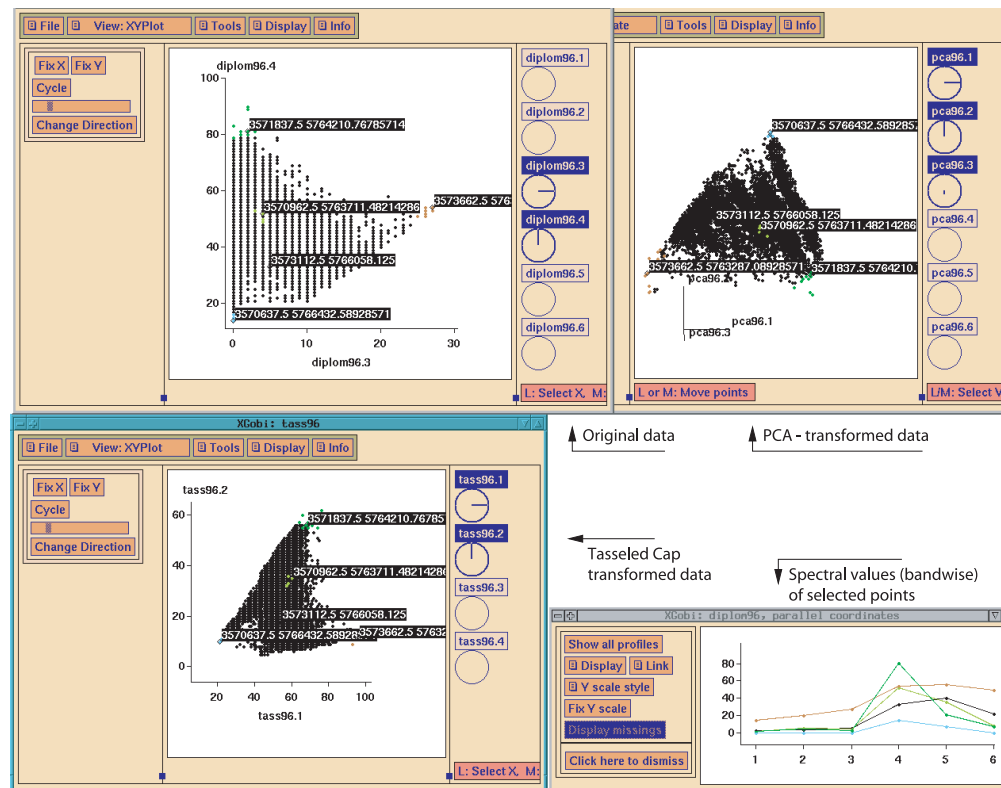
Figure 8: XGOBI multi-session with interprocess communication enabled. The user can select endmembers for spectral unmixing in the extremities of the data clouds (here PCA and Tasselled Cap transform) and analyse the spectra in the parallel plot window
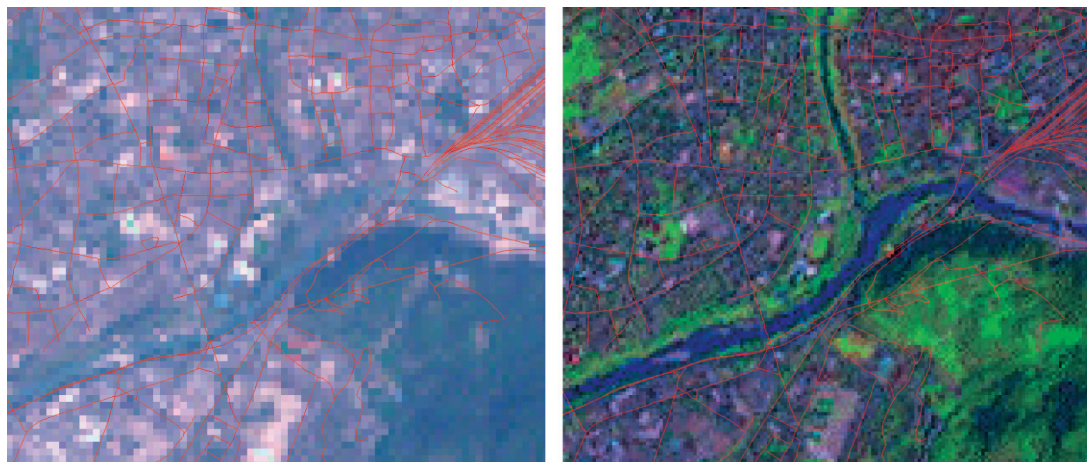


Figure 9: Left: LANDSAT-7 RGB composite at 28.5m; right: LANDSAT-7 RGB/PAN Brovey fusion at 14.25 m

iteration is performed until no further significant change appears in the error minimisation. In Figure 6, the search for the optimal solution can be seen as moving towards the minimum. To spectrally unmix an image scene, this method must be applied to all pixels.

The spectral unmixing is usually based on a spectral library containing a large set of laboratory spectra or is done with a geometrical search for "pure" spectra in the image scene. A geometrical search can be done by various methods, such as using Principal Component Analysis (PCA). Endmembers ("pure" spectra) are located in the extremities of the PCA-transformed multidimensional pixel cloud. They can be extracted interactively with *XGOBI* software (Swayne et al., 1998). This software supports interprocess communication (IPC), which enables the user to run several program sessions in parallel while the sessions maintain communication. The user can interactively query transformed and untransformed data in either session for the identification of endmembers, pixel map coordinates are indicated in all *XGOBI* windows (Figure 8). From these coordinates pure pixels can be easily extracted and used as endmembers. From the created endmember file (either from a spectral library or from geometrical search within the image scene) the spectral unmixing is performed. The result is a set of endmember abundance maps describing pixel wise the area percentage of each endmember. The algorithm is implemented in *i.spectral.unmix.*

## 4. Image Fusion with Brovey Transform

In remote sensing systems parts of the spectrum are observed in different portions to minimise the impact of noise. While multispectral sensors provide high spectral resolution at lower spatial resolution, panchromatic sensors collect data at high spatial resolution and lower spectral resolution. Numerous algorithms have been proposed to combine these data with best characteristics of both sensor types. One of these algorithms, the Brovey transform, has

been selected for script based implementation in GRASS. The Brovey transform is a colour transform which normalises three input bands and multiplies the result with a higher resolution band (panchromatic) (Roller and Cox, 1980; Pohl and van Genderen, 1998):

$$DN_{fused} = \frac{DN_{b1}}{DN_{b1} + DN_{b2} + DN_{b3}} \cdot DN_{pan}$$

Equation 16

The Brovey algorithm holds an intermediate position between band arithmetic and component substitution methods. A new script *i.fusion. brovey* has been integrated to GRASS to support PAN sharpening of multispectral satellite such as that from LANDSAT-7, Quickbird and SPOT. The algorithm performs image fusion of the high resolution panchromatic channel with the multispectral channels at lower resolution. The resulting pseudo-RGB channels are saved at the high resolution of the panchromatic channel and have a near-natural colour table. An example of LANDSAT-7 fusion is shown in Figure 9.

## 5. High Performance Image Classification on OpenMosix Cluster

A high performance solution for image classification with GRASS at meso-scale but with high spatial resolution was developed. A script-based approach to run the standard, unmodified GRASS on an GNU/Linux based *openMosix* cluster (20 PCs, 40 CPUs) has been implemented to classify multispectral colour orthophotos with SMAP algorithm (Sequential maximum a posteriori estimation, Bouman and Shapiro, 1994; Schowengerdt, 1997). *openMosix* (http://www.openmosix.org, published under GPL) is a Linux kernel extension for single system image clustering. Once *openMosix* is installed and the cluster nodes are connected by a local network, the nodes in the cluster communicate to optimally distribute the workload. Processes originating from any node can migrate to any other node if the current node is too busy compared to others. *openMosix* con-

59

tinuously attempts to optimise the resource allocation. New nodes can be added while the cluster is running and the cluster will automatically begin to use the new resources. Due to the distributed computing concept of *openMosix,* the cluster behaves similar to a symmetric multi-processor (SMP). In order to run GRASS in parallel without code modifications, a multiple sequential approach was used. Within the job launch script the GRASS environment variables are defined. It is important to run each job in its own mapset to avoid one job influencing the settings of another job. The definition section is followed by the GRASS analysis (in our case the SMAP classification). To finish, the launch script removes the temporary files and copies the resulting classification map to the PERMANENT mapset. It uses UNIX commands as the original *g.copy* command may fail due to race conditions (in this case the concurrent writing of files) with other jobs copying results to the PERMANENT mapset at the same time. The approach was tested on a large study area, the Autonomous Province of Trento (Italy), which is of approximately 6200 km$^2$ area. This area is covered by 280 RGB orthophotos at a resolution of one meter per pixel (Volo Italia 2000, CGR Parma). In tests, the required time to analyse these orthophotos at the given resolution was reduced from estimated 110 days on a single CPU to 5 days on the ITC-irst *openMosix* cluster.

## Acknowledgements

## References

Bouman, C. and Shapiro, M., 1994, A multiscale random field model for Bayesian image segmentation. *IEEE Transactions on Image Processing,* 3, 2, 162-177.

Chambers, J., Cleveland, W., Kleiner, B., and Tukey, P., 1983, *Graphical methods for data analysis,* (Chapman & Hall).

Grasso, D., 2004, *Registrazione di immagini telerilevate mediante strutture lineari e ground control points.* Master's thesis, University of Trento, Italy.

Hobbs, S., 1996, Linear mixture modelling solution methods for satellite remote sensing. *Technical Report 9603,* COA, Bedford.

Keshava, N. and Mustard, J., 2002, Spectral Unmixing. *IEEE Signal Processing,* 19(1), 44-57.

Michelazzi, I., 2004, *Geocodi ca ed elaborazione di immagini oblique per visualizzazione 3D in ambiente GIS.* Master's thesis, University of Trento, Italy.

Miori, L., 2004, *Tecniche automatiche per la co-registrazione di immagini telerilevate.* Master's thesis, University of Trento, Italy.

Murino, V., Castellani, U., Etrari, A., and Fusiello, A., 2002, Registration of very time-distant aerial images. *Proceedings of the IEEE International Conference on Image Processing* (ICIP 2002, Rochester, NY, Sept. 22-25), III, 989-992.

Neteler, M., 1999, *Spectral Mixture Analysis von Satellitendaten zur Bestimmung von Bodenbedeckungsgraden im Hinblick auf die Erosionsmodellierung.* Master's thesis, University of Hannover, Germany.

Neteler, M. and Mitasova, H., 2004, *Open Source GIS: A GRASS GIS Approach. 2$^{nd}$ edition,* (Boston: Kluwer Academic Publishers).

Pohl, C. and van Genderen, J., 1998, Multisensor image fusion in remote sensing: concepts, methods and application. *International Journal of Remote Sensing,* 19, 823-854.

Roller, N. and Cox, S., 1980, Comparison of Landsat MSS and merged MSS/RBV data for analysis of natural vegetation. *Proceedings of the 14th International Symposium on Remote Sensing of Environment,* 1001-1007.

Schowengerdt, R., 1997, *Remote sensing: Models and methods for image processing, 2nd edition,* (Academic Press).

Shaw, G. and Manolakis, D., 2002, Signal processing for hyperspectral image exploitation. *IEEE Signal Processing,* 19(1), 12-16.

Shimabukuro, Y. and Adams, J., 1991, The least-squares mixing models to generate fraction images derived from remote sensing multi-spectral data. *IEEE Transactions on Geoscience and Remote sensing,* 29(1), 16-20.

Sohn, Y. and McCoy, R., 1997, Mapping desert shrub rangeland using spectral unmixing and modeling spectral mixtures with TM data. *Photogrammetric Engineering & Remote Sensing,* 6(6), 707-716.

Swayne, D., Cook, D., and Buja, A., 1998, X Gobi: Interactive dynamic data visualization in the X Window System. *Journal of Computational and Graphical Statistics,* 7(1), 47-67.

Wolf, P., 1983, *Elements of Photogrammetry with Air Photo Interpretation and Remote Sensing.* 2nd edition, (New York: McGraw-Hill).